Journal of African Earth Sciences 57 (2010) 249–261

Contents lists available at ScienceDirect

Journal of African Earth Sciences

journal homepage: www.elsevier.com/locate/jafrearsci

Mn oxides as efficient traps for metal pollutants in a polyphase low-temperature Pliocene environment: A case study in the Tamra iron mine, Nefza mining district, Tunisia

Sophie Decrée [a,b,*], Gilles Ruffet [c], Thierry De Putter [b], Jean-Marc Baele [d], Philippe Recourt [e], Fakher Jamoussi [f], Johan Yans [a]

[a] Facultés Universitaires Notre-Dame de la Paix – FUNDP, Département de Géologie, 61 rue de Bruxelles, 5000 Namur, Belgium
[b] Musée Royal de l'Afrique Centrale, Géologie Générale, 13 Leuvensesteenweg, B-3080 Tervuren, Belgium
[c] Géosciences Rennes, UMR CNRS 6118, Campus de Beaulieu, Université de Rennes1, 35042 Rennes Cedex, France
[d] Faculté Polytechnique de Mons, Géologie Fondamentale et Appliquée, 9 rue de Houdain, B-7000 Mons, Belgium
[e] Université des Sciences et Techniques de Lille 1, Laboratoire Géosystèmes (UMR 8157 CNRS) UFR des Sciences de la Terre – bâtiment SN5 59655 Villeneuve d'Ascq cedex, France
[f] Centre de Recherche et de Technologie des Eaux. Technopole de Borj-Cédria – Route touristique de Soliman BP 273-8020 Soliman, Tunisia

ARTICLE INFO

Article history:
Received 16 December 2008
Received in revised form 6 August 2009
Accepted 21 August 2009
Available online 6 September 2009

Keywords:
Ar dating
Chalcophanite
Coronadite
Nefza
Tamra
Tunisia

ABSTRACT

The Tamra mine, located in the Nefza mining district (NW Tunisia), exploits a 50 m-thick layer of Mio-Pliocene sediments that are heavily mineralized with Fe and other metals (Mn, Pb, Zn), especially in its eastern part, which is highly mineralized in Mn and known as the "manganiferous zone". The textural and geochemical studies of manganiferous minerals in the Tamra mine have allowed the determination of four main paragenetic stages. Stages 1 and 2 relate to the main pedogenetic event that gave rise to the currently exploited Fe ore deposit. The last two stages relate to mineralizing events closely connected with hydrothermal circulation and leaching of underlying mineralization of the Sidi Driss Pb–Zn sedex deposit, with subsequent crystallisation in the supergene environment. Stage 3 is characterized by the formation of massive romanechite, hollandite and Sr-cryptomelane, while stage 4 results in the formation of coronadite and chalcophanite. ^{39}Ar–^{40}Ar analyses performed on hollandite (stage 3) and coronadite (stage 4) samples yielded ages of 4.7 ± 0.1 Ma and 3.35 ± 0.07 Ma, respectively. Tentative ^{39}Ar–^{40}Ar analyses on chalcophanite provided aberrant results, due to the poor argon retention in this layer-structure mineral. The youngest age corresponds to the late phase of the late Alpine extension event in northern Tunisia, evidenced through an increased regional thermal gradient as well as by a N–S set of normal faults and fractures. The Tamra mine is obviously a polyphase mineral deposit, recording several distinct metal inputs, part of them originating from the underlying Sidi Driss Pb–Zn deposit, while another part is provided by hydrothermal circulations forced by the high thermal gradient.

Three springs flowing from the Tamra ore series are regular sources for drinking water used by the local population. Although the Alpine thermal gradient could have facilitated extensive mixing between subsurface oxidizing meteoric fluids and deep reducing hydrothermal tepid fluids, the springs flowing out in the Tamra mine are not significantly polluted with metallic elements (Fe, Pb, Zn, Mn), and can be regarded as drinking waters according to the World Health Organization (WHO) standards. ^{39}Ar–^{40}Ar ages suggest that complex Mn oxides formed early in the deposit history. These oxides incorporated metal ions in their mineral structure and/or acted as high-surface-area substrates favouring heavy metal adsorption (e.g. Pb on Mn oxides). Similar adsorption/co-precipitation processes are also exhibited by iron oxides, which form the major part of the Tamra sediments. These efficient trapping processes most probably account for a restricted migration of "pollutants" through the neighbouring sediments and the circulating fluids.

1. Introduction

In the Nefza region that belongs to the Nappe Zone of northern Tunisia, small post-nappe basins host minor Pb–Zn and Fe mineralizations. The Tamra iron mine is the last open pit still active today. While mining the Tamra open pit, a Mn-rich area was recognized (hereafter referred to as Mn-zone = manganiferous

* Corresponding author. Address: Facultés Universitaires Notre-Dame de la Paix – FUNDP, Département de Géologie, 61 rue de Bruxelles, 5000 Namur, Belgium. Fax: +3281724478.
E-mail addresses: sdecree@fundp.ac.be, sofie.decree@africamuseum.be, sdecree@hotmail.com (S. Decrée), gilles.ruffet@univ-rennes1.fr (G. Ruffet), thierry.de.putter@africamuseum.be (T.D. Putter), Jean-Marc.Baele@fpms.ac.be (J.-M. Baele), philippe.recourt@univ-lille1.fr (P. Recourt), fakher.jamoussi@certe.rnrt.tn (F. Jamoussi), johan.yans@fundp.ac.be (J. Yans).

1464-343X/$ - see front matter © 2009 Elsevier Ltd. All rights reserved.
doi:10.1016/j.jafrearsci.2009.08.005

zone) (Negra, 1987; Bouzouada, 1992), meaning that it was mined as Mn ore in the past.

The purpose of this study is to determine the role of the Mn-rich minerals in the trapping of the pollutant elements present in the mine, i.e. mostly Pb and Zn (Decrée et al., 2008a); such a role is well-known in the literature, either by co-precipitation, adsorption or complexation (Manceau et al., 1992; Dong et al., 2000; Feng et al., 2007). This is of special interest for the understanding of potential health problems linked to water supply in the studied mining district, as fluids flowing out the Tamra mine are regarded as drinkable water for local communities. A similar study dedicated to the impact of mining activities on the surface waters from the "Oued Mellègue" river and its tributary streams, several tens of kilometres to the SW of the Nefza district (Fig. 1a), has been realised by Mlayah et al. (2009). These authors have investigated tailings of Pb–Zn–Ba and Fe mines, and performed stream-sediment analyses they interpreted by principal component analysis (PCA). Their aim was to evaluate the efficiency of the different components: (1) regional substrate rocks; (2) fine-grained ore mineral particles ("micro-phases"); and (3) hydrated oxihydroxide components, in trapping heavy metals.

Our study differs by several aspects from the Oued Mellègue study: the Tamra system is a small-scale system where the three components identified by Mlayah et al. (2009) are in fact the ore itself.

The present study will further contribute to a better understanding of the mineralization processes observed in the Tamra sediments, in relation with pan-regional geodynamic events; this approach will benefit by Ar dates, obtained on Mn oxides. During the last decade, $^{40}Ar/^{39}Ar$ laser probe step-heating analyses on Mn oxides have been widely used to constrain the geochronology of weathering phases all around the world (Vasconcelos et al., 1995): in Australia (e.g. Dammer et al., 1999; Li and Vasconcelos, 2002), in Europe (e.g. Hautmann and Lippolt, 2000), in Asia (e.g. Li et al., 2007), in America (e.g. Vasconcelos et al., 1992; Ruffet et al., 1996; Chan et al., 2001; Mote et al., 2001; Spier et al., 2006) and in Western Africa (Hénocque et al., 1998 ; Colin et al., 2005; Beauvais et al., 2008). This paper presents the first dating of supergene K–Mn oxides from North Africa.

2. Geological context

The study area is located in north-western Tunisia, a few kilometers to the north of the town of Nefza (Fig. 1a), which was known in the first half of the 20th century as a mining district center. It is part of the widespread Northern Tunisian "Nappe Zone" (Rouvier, 1977; Rouvier et al., 1985; Fig. 1a), composed of thrust sheets. In the studied area, the nappe pile is made of the Ed Diss thrust sheets (Upper Cretaceous to Eocene, alternating limestones and marls), overlain by the Numidian nappe (Rouvier, 1977) (Fig. 1b). The latter consists of a thick ($\geqslant$1000 m) series of silicoclastic flyschs (the so-called Numidian flysch, made up of sandstones and argilites), Oligocene to Burdigalian in age.

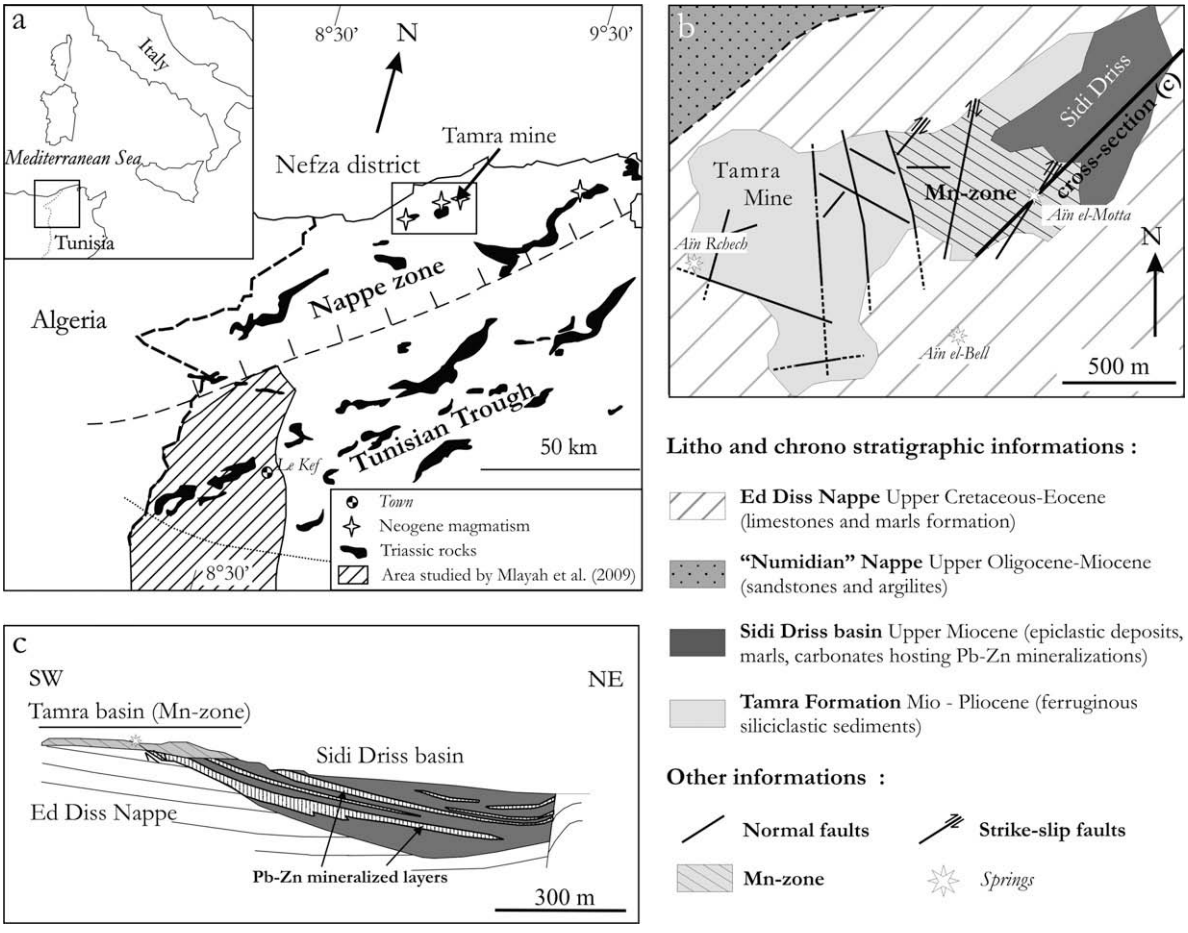

Fig. 1. Location maps (a) of the studied site within the main tectono-sedimentary units (modified from Rouvier et al. (1985)) and (b) showing the regional units in the vicinity of the Tamra mine, the different parts of the manganiferous zone and the location of the three studied springs. Schematic cross-section of the Sidi Driss-Tamra zone (c); this section (located in Fig. 1b) is modified after Stefanov and Ouchev (1972); in Dermech (1990) and Decrée et al. (2008b).

The Tamra Mio-Pliocene sediments, which fill up the post-tectonic Tamra basin, have been described in a detailed sedimentological, mineralogical and geochemical study (Decrée et al., 2008a). It consists of a 50 m-thick series of heavily Fe mineralized stratiform deposits made up of sequences tentatively grouped into a schematic lithological log (Fig. 4. in Decrée et al., 2008a). These sequences comprise dominantly siliciclastic units. Each sequence is being topped by a paleosoil horizon witnessing emersive conditions. These sediments were deposited during a short period ranging from Late Miocene to Early Pliocene, under a regional extensional tectonic regime (Bouaziz et al., 2002), favourable for sedimentary record deposition and preservation (Decrée et al., 2008a).

The Tamra iron ore results from a combination of: (i) pedogenetic pre-concentration processes, linked to interaction with meteoric fluids feeding temporary aquifers, which are involved in seasonal Fe concentration processes (Decrée et al., 2008a) and (ii) hydrothermal Fe enrichment (Decrée et al., 2008a).

The Mn mineralization studied in this paper pertains to the so-called manganiferous zone (hereafter MZ); in the eastern part of the Tamra mine (Fig. 1b). The iron ore from the Mn-zone is characterized by an important Mn content, as well as by positive anomalies in Pb, Zn, Sr and Ba. The enrichment in these elements is attributed to hydrothermal fluid circulations, which have migrated through the underlying Sidi Driss basin (Fig. 1c). This basin is indeed hosting a Sedex-type Messinian sulfide deposits (galena, sphalerite and marcasite) within primary sulfates (barite and celestite) and Fe–Mn dedolomite (i.e. calcite pseudomorph after dolomite, retaining the rhomb shape of dolomite) (Decrée et al., 2008b). Such enrichments in Mn, Pb, Zn, Sr, Ba have also been observed to the west of the Mn-zone, though restricted to late subvertical N–S and NW–SE trending mineralized normal faults, cross-cutting the whole series. Pyrite, siderite and galena crystallized in these distal veins, while galena and sphalerite associated with psilomelane (=romanechite) $[(Ba,H_2O)_2(Mn^{4+},Mn^{3+})_5O_{10}]$ are found in the Mn-zone (Bouzouada, 1992).

Regional hydrothermal circulations allowing for such migration and enrichment processes are assumed to take place from the Messinian period onward, probably in connection with Late Miocene magmatic activity (Decrée et al., 2008b). Tepid thermal fluids flowing presently in Nefza town and in the Sidi Driss basin (Stefanov and Ouchev, 1972) have also been observed, flowing at low discharge rates, in the Sidi Driss basin (Zouiten, 1999; Decrée et al., 2008a). They result from a high thermal gradient (over 10 °C/100 m associated with the presence of a shallow level magmatic sill whose emplacement benefited from lithospheric weakness and a zone of deep-seated fractures (Jallouli et al., 1996). These tepid springs have kept flowing for decades, because the area experiences a high annual rainfall (1000–1500 mm/yr; Stambouli-Essassi et al., 2007), constantly feeding the regional aquifers.

Three springs are flowing out in the Tamra mine (see location on Fig. 1b): "Aïn el-Motta" spring located close to the Mn-zone, "Aïn el-Bell" spring located to the south of the mine, and "Aïn Rchech" spring, the latter flowing out at the contact between the ore and the impervious marls of the Ed Diss bedrock, in the westernmost part of the mine. The three springs (sampled in September 2004) are weakly acidic (pH around 5–6 as measured in the field), and exhibit quite coherent chemical characteristics with low Fe (1.4–7.7 ppb), Mn (1.1–3.9 ppb) and Pb (0.3–1.2 ppb) contents, whereas Zn content is high in the three springs (25–297 ppb), as are also Ba (79.1–142 ppb) and Sr (333–2400 ppb) contents. These values are however well below the guideline values (for Mn, Pb and Ba) or recommended values (for Fe and Zn) for these metal contents in drinking water (2000 ppb for Fe, 400 ppb for Mn, 10 ppb for Pb, 300 ppb for Zn, 700 ppb for Ba, as recommended by WHO (http://www.who.int/water_sanitation_health/dwq/gdwq0506_12.pdf). These low metal concentrations therefore exclude the problem of saturnism or manganism (Bouchard et al., 2007) for local populations. No WHO guideline values are available for Sr; however our data are in the range of the Sr content in Italian bottled mineral waters (in which Sr contents reach 14.7 ppm; Naddeo et al., 2008).

3. Sampling methodology

Seventeen rock samples that seemed to contain Mn oxides were collected in 2004 from the Tamra mine. Twelve of them came from the most distal (i.e. distant from the inferred source at Sidi Driss) part of the manganiferous zone (=Manganese Zone Distal, or MZD) and were taken along a profile (Fig. 2). Five more were sampled in the proximal Mn zone (Manganese Zone Proximal, or MZP), ~10 m below the surface.

The samples have been powdered for X-ray micro-diffraction (XRD) analyses and convenient pieces were prepared in polished sections for environmental scanning electron microscope (ESEM) observation and semi-quantitative chemical analyses.

These mineralogical investigations were carried out to determine the mineralization processes and to select convenient Mn oxides samples for Ar–Ar dating.

To perform such analyses, the samples containing the more massive and homogeneous Mn oxides have been roughly crushed to obtain millimeter-wide fragments. The most homogeneous fragments were carefully handpicked under a binocular microscope and pasted onto a support to be observed with the ESEM. The aim of the latter examination was to check the homogeneity of

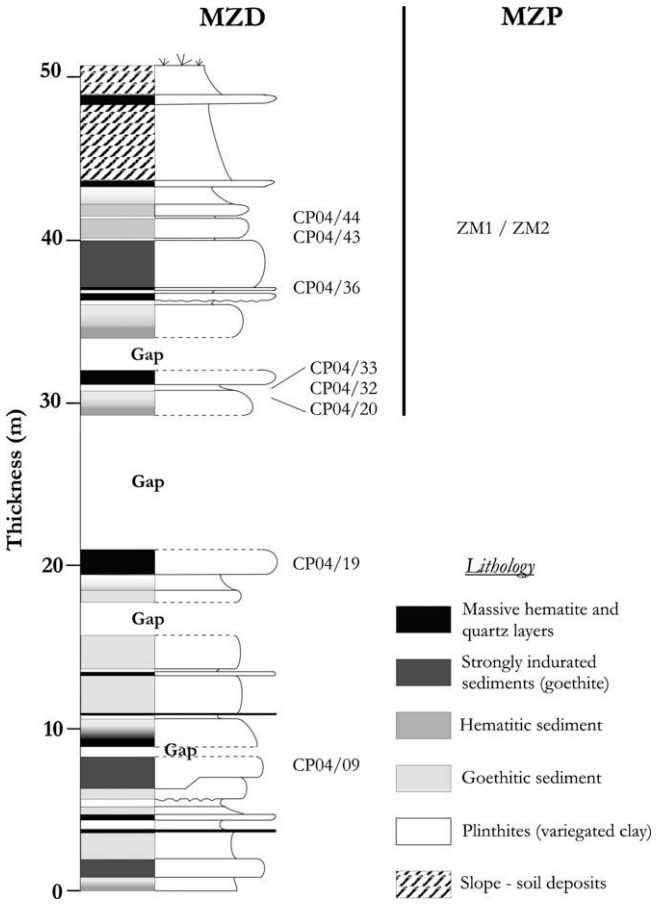

Fig. 2. Location of the studied samples in the lithological log of the Tamra quarry (Decrée et al., 2008a).

the samples, and to select the most uniform fragments on which to perform Ar–Ar analyses.

In this way, four samples of Mn oxides were chosen and investigated for ^{39}Ar–^{40}Ar dating (see Table 1).

4. Mineralogical characterisation of the samples

The mineralogy of the rock samples was determined with: (i) a Bruker–Siemens X-ray micro-diffraction instrument equipped with a Cu Kα X-ray tube (operating at 40 kV and 30 mA), and a General Area Detector Diffraction System (GADDS) detector system at the "Laboratoire de Géochimie et Minéralogie appliquée" (Université Libre de Bruxelles) and (ii) an environmental scanning electron microscope (ESEM FEI Quanta 200) at the Université of Lille 1. This microscope is equipped with an energy dispersive X-ray spectrometer (EDS Quantax QX2 Roëntec X Flash 3001), and was also used to make the quantitative analysis (bulk of a few mm^3). As the samples were analysed without any carbon coating, the low vacuum mode was used (0.5 torr). Analyses were carried out on powdered samples and polished sections, at 20 kV, with a counting time of 100 s, and at a working distance of 12–15 mm. The absence of carbon coating can occasionally induce some contamination of the analyzed spot by surrounding minerals, especially for metallic phases.

XRD and ESEM examination of samples collected in the MZ shows that romanechite, hollandite, coronadite and chalcophanite are the dominant Mn-bearing mineral phases (Table 2, Fig. 3). A Sr-rich Mn oxide (from 2.7% to 4.7% SrO) was also recognized. Its XRD pattern is very close to the cryptomelane pattern (much more than to the strontiomelane pattern; Fig. 3a), despite its low K-content (0.8–1.7% K_2O, Tables 3 and 4). This strontian Mn oxide, diffracting as a cryptomelane, is hereafter called Sr-cryptomelane. Mn–Pb oxide is also deduced from EDS analyses (Tables 3 and 4); its amorphous character is inferred from the lack of diffraction pattern, though the absence of XRD pattern could result as well from the low abundance of this phase. The distinction between the two Ba–Mn oxides (romanechite and hollandite) is reasonably easy due to their different XRD patterns (Fig. 3b, c and d). On the contrary, the hollandite and coronadite patterns are not easily distinguishable (Fig. 3e) as they belong to the same "hollandite" group (Post, 1999). This group, with a type-formula $[R_{0.8-1.5}(Mn^{4+}, Mn^{3+})_8O_{16}$ R = Ba, Pb, K], allows for extensive solid solutions between its "end-members". Actually, the structural tunnel of the "hollandite" group incorporates large cations such as Ba^{2+}, Pb^{2+}, K^+: hollandite *sensu stricto* (Ba), cryptomelane (K), coronadite (Pb). The solid solution can even include strontiomelane (Schreyer et al., 2001). This explains why most of the observed Mn oxides in the studied material contain significant quantities of Sr.

The identification of chalcophanite is rather straightforward from its well defined XRD pattern (Fig. 3f) and its high Zn content (ESEM examination).

5. Textural relationships, paragenesis and oxide geochemistry

A paragenetic sequence was developed from hand specimens and thin section examination. The different stages of the sequence were defined primarily by Mn oxide speciation and secondarily by Fe oxide facies/texture.

The four paragenetic stages (Fig. 4) are:

(1) Mn oxides (and other pollutants) mixed within and/or adsorbed onto soft Fe oxide matrix.
(2) Mn oxides (and other pollutants) mixed within and/or adsorbed onto Fe concretions.
(3) (Ba, Sr, K)-rich Mn oxides crystallized in voids within Fe concretions or enclosing Fe oxide grains.
(4) Dominant (Pb, Zn)-rich Mn oxides crystallizing in remaining open voids.

Mn oxides of stages 1 and 2 are volumetrically minor but are present in the entire Tamra mine (i.e. also out of the MZ), whereas stages 3 and 4 Mn oxides occur as massive Mn-bearing concretions, the major part of Mn oxides found in the eastern part of the MZ. For these two later stages, it is possible to differenciate unambiguously the two above-mentioned sub-zones: MZP, significantly enriched in those elements originating from Sidi Driss: Mn, Pb, Zn, Sr; Decrée et al., 2008b; and MZD, less enriched in these elements. The distinction between the two sub-zones is thus based on both geographical locations and mineralogical characteristics.

Stage 1 includes those Mn oxides filling the porosity in the ferruginous matrix (which is composed of iron oxides, kaolinite and quartz), either by impregnation or through adsorption/co-precipitation. The MnO content of the Fe matrix ranges from 1% to 6.1% (Tables 3 and 4), with local enrichment in Zn (up to 4.8% Zn) (Tables 3 and 4). In this early stage of evolution, the soft/poorly indurated iron oxides acted as a "spongy" reservoir allowing the adsorption of elements carried by hydrothermal fluids, and as a substrate onto which Mn-bearing oxide minerals could grow. Stage 1 is therefore likely to be a pre- or syn-pedogenetic stage (Decrée et al., 2008a).

Stage 2 corresponds to the formation of typical ferruginous concretions/boxworks where the Mn oxides are intimately mixed with iron oxides (C in Fig. 5a: 17.8–39.1% MnO; Tables 3 and 4). These concretions show Pb and Zn enrichments (up to 14.6% and 1.7–11.8%, respectively; Tables 3 and 4) compared to the host soft ferruginous matrix, and exhibit low BaO, SrO and K_2O contents (up to 3.2% for the three oxides sum; Tables 3 and 4). The formation of mixed Fe(–Mn) concretions was identified as the main Fe concentration process, during the main pedogenetic event (Decrée et al., 2008a). Iron concretions result from a combined reworking process of iron from the initial stock in the spongy matrix (stage 1) and interaction with downward percolating meteoric fluids with episodic waterlogging. The same processes were probably active for Mn as well, since this metal is known to be highly mobile in oxidizing systems (Stumm and Morgan, 1996; Appelo and Postma, 1994), and for other elements recycled from the matrix, such as Pb and Zn.

Stage 3 is characterized by the deposition of massive (Ba, Sr, K)-bearing Mn oxides.

In the MZP, romanechite and hollandite (determined by XRD) are the most abundant Mn oxides, forming massive Mn concretions/ore. They occur as void and fracture fillings within the stage 2 mixed Fe–Mn concretions (Fig. 5a), sometimes forming dendrites within the goethitic matrix, and/or as homogeneous ore (Fig. 5b; sample ^{39}Ar–^{40}Ar ZM2cc2) incorporating goethite grains or grain aggregates.

In the MZD, massive Mn oxide ore is mainly comprised of hollandite surrounding iron oxide grains and incorporating iron oxide aggregates (Fig. 6a).

Whatever the sub-zone of the mine, stage 3 mineral phases exhibit lower Pb and Zn contents (2.4–4.3% and 3.1–9%; Tables 3 and 4) and, as expected, enrichment in Ba, Sr and K contents (up to 5.8% BaO (in the MZP), 4.7% SrO and 1.7% K_2O; Tables 3 and 4) when compared to the ferruginous concretions. The stage 3 minerals are also sometimes mixed with residual iron (up to 8.8% FeO; Tables 3 and 4). Since the stage 3 Mn concretions are observed filling fractures within former Fe–Mn concretions (or voids within these), and involved very little Fe remobilization, they are interpreted as "late", post-pedogenetic phases.

Stage 4 relates to late crystallization of Pb–Zn enriched Mn oxides (up to 30.5% PbO, up to 21.1% ZnO, up to 3.5% BaO + SrO + K_2O;

Table 1
Overview of the 17 studied samples within their zones, of their nature and of the analytical methods used to characterize and investigate them.

Zone	Sample	Description	Analyses
Distal Manganese Zone (MZD)	CP 04/09	Goethitic concretion	XRD, ESEM (Decree et al., 2008a)
	CP 04/19	Massive hematite + quartz bars	XRD, ESEM (Decree et al., 2008a)
	CP 04/20geod	Goethitic concretion	XRD, ESEM
	CP 04/20 cc	Mn concretion within CP 04/20 geod.	XRD, ESEM, ^{39}Ar–^{40}Ar
	CP 04/32	Goethitic matrix	XRD, ESEM
	CP 04/32geod	Concretion within CP 04/32	XRD, ESEM
	CP 04/33	Concretion	XRD, ESEM
	CP 04/36	Massive hematite + quartz bars	XRD, ESEM (Decree et al., 2008a)
	CP 04/43	Goethitic matrix	XRD, ESEM
	CP 04/43geod	Geode infilling wihin CP 04/43	XRD, ESEM
	CP 04/43 cc	Concretion within CP 04/43	XRD, ESEM, ^{39}Ar–^{40}Ar
	CP 04/44	Mixed Fe–Mn concretion	XRD, ESEM
Proximal Manganese Zone (MZP)	ZM1	Goethitic matrix and concretions	XRD, ESEM
	ZM1cc1	Mixed Fe–Mn concretion within ZM1 m	XRD, ESEM
	ZM1cc2	Massive Mn concretion within ZM1 m	XRD, ESEM
	ZM2cc1	Mixed Fe–Mn concretion	XRD, ESEM
	ZM2cc2	Massive Mn concretion	XRD, ESEM, ^{39}Ar–^{40}Ar

Table 2
Formula of the Mn oxides encountered in the Tamra mine.

Mineral name	Formula
Strontiomelane	$SrMn^{4+}{}_6Mn^{3+}{}_2O_{16}$
Cryptomelane	$K_{1-1.5}(Mn^{4+},Mn^{3+})_8O_{16}$
Hollandite	$Ba(Mn^{4+},Mn^{2+})_8O_{16}$
Coronadite	$Pb(Mn^{4+},Mn^{2+})_8O_{16}$
Romanechite	$(Ba,H_2O)_2(Mn^{4+},Mn^{3+})_5O_{10}$
Chalcophanite	$(Zn,Fe^{2+},Mn^{2+})Mn^{4+}{}_3O_7{\cdot}3(H_2O)$

Tables 3 and 4), which are coronadite, amorphous Pb–Mn oxides and chalcophanite that crystallized within and/or around stage 3 Mn geodes.

In the MZP, coronadite mainly occurs as μm-thick rim underlining the edge between massive hollandite and goethite grains (Fig. 5b) or as a dense network of needles (with needles up to 30 μm in length, Fig. 5c) within tiny fissures/fractures interpenetrated with felted hollandite. In other fissures of this sub-zone, felted chalcophanite displays intergrowth with romanechite (Fig. 5d). The coexistence of various mineral phases within tiny fissures suggests a co-precipitation process, responding to very local chemical variations occurring in restricted volumes.

In the MZD, similar coronadite needles (up to 100 μm in length preserved within Sr-cryptomelane, Fig. 6a) underline the edges between iron oxide grains and aggregates within massive Mn oxide (in this case, Sr-cryptomelane). Coronadite also impregnates iron oxide aggregates, fills tube-like voids (Fig. 6b) and form massive millimetre-thick concretions (sample ^{39}Ar–^{40}Ar CP04-20 cc) after hollandite. However, mammillary coronadite (or amorphous Pb–Mn oxide; Fig. 6c and d) constitutes the more typical Mn concretions in the MZD. These latter concretions apparently grew through *per descensum* process, and are generally connected with an overlying dense tubule network (within the ferruginous ore) that possibly enhanced the downward percolation of Mn-bearing fluids. Some of these oxides crystallized in close association with a kaolinite horizon (K in Fig. 6d), and are therefore intimately mixed with the clay minerals. Most of the Pb–Mn oxides are rimmed by a thin iron oxide lining (Fig. 6c and d). Iron oxide also partially fills late-formed contorted tube-like cavities crosscutting the Pb–Mn oxides (Fig. 6d). Needle-like crystals of coronadite (Fig. 6e) are also lining (mammillary) chalcophanite fan-like flakes (sample ^{39}Ar–^{40}Ar, CP04–43 cc).

Another distinctive coronadite texture is shown in Fig. 6f where this mineral is finely interbedded with iron oxide linings or cauliflower structures. The latter structures are similar in size and shape to microstromatolites (Boulvain, 1989) and bush-like calcimicrobes (Flügel, 2004). They are therefore of probable biogenic origin and suggest that mineral processes were bacterially mediated since many chemical reactions, including Fe and Mn oxidation/reduction, are of vital metabolic importance for a number of chemo-autotrophic microorganisms (Ehrlich, 2002).

6. Interpretation in terms of hydrothermal and chemical evolutions

In this complex mineralized system, we assume that the observed geochemical variations reflect changes in the provenance of elements, which mainly derive from either the host rock or the incoming hydrothermal fluids (with variable chemistry depending on the position in the manganiferous zone: MZP or MZD). We have plotted the content in PbO, ZnO, BaO, SrO and K_2O measured in several minerals/mineral association for each stage (Tables 3 and 4; Fig. 7a), and observed that stage 2 records a (Pb, Zn) enrichment when compared to stage 1. This enrichment is regarded as a reconcentration of elements from the soft ferruginous matrix (as described above), where extra Pb and Zn input linked to hydrothermal activity cannot be ruled out. Stage 3 minerals are characterized by a significant increase in Ba, Sr and (to a lesser extent) K contents (Fig. 7a and b), but a lowering of Pb and Zn contents, that are unlikely to result from a reconcentration process from earlier concretions (Ba, Sr, K poor and Pb, Zn rich). This suggests that (Pb, Zn)-poor hydrothermal fluids brought Ba, Sr and K in the Tamra sediment at the stage 3 time. Stage 4 corresponds to a "late" and significant Pb-(Zn-) mineralizing event, marked by a sharp increase in Pb content within Mn concretions (inducing coronadite formation), together with a more restricted and localized Zn input (causing chalcophanite crystallization), and a correlative decrease in BaO, SrO and K_2O (Fig. 7a and b) contents. The high Pb and Zn contents in this stage most probably result from hydrothermal input rather than from a reconcentration from former deposits. However, the co-precipitation of hollandite with coronadite (or romanechite with chalcophanite) probably points to a very local destabilization of stage 3 Mn oxides by late Pb–Zn rich fluids.

7. ^{39}Ar–^{40}Ar analyses

Four Mn-oxide samples were investigated for ^{39}Ar–^{40}Ar dating analyses: a romanechite (ZM1cc2), a hollandite (ZM2cc2), a

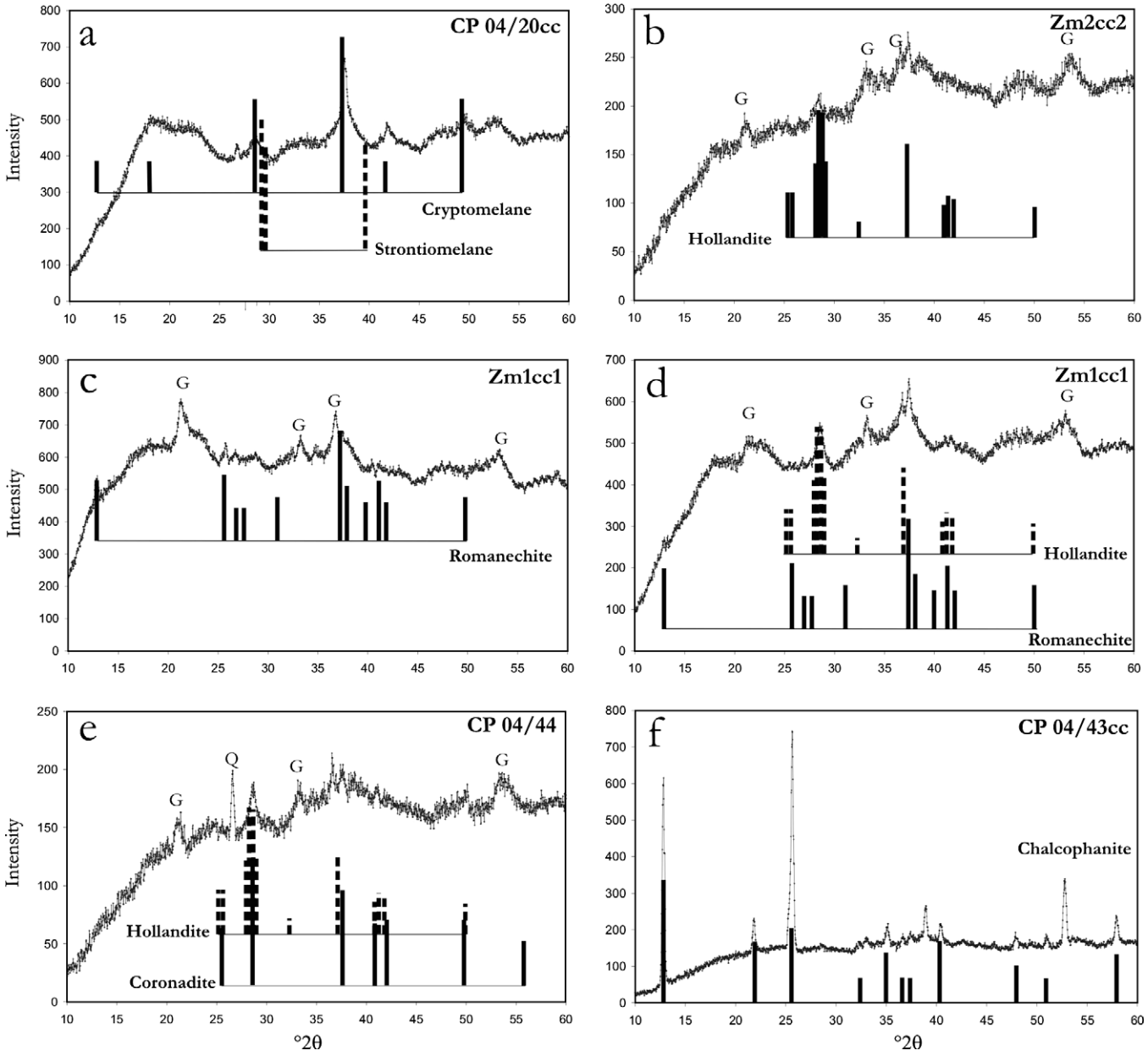

Fig. 3. XRD patterns (Cu Kα) of representative Mn concretions in the Tamra mine compared to the reference patterns (vertical lines) from the "International Centre for Diffraction Data" database (using EVA Bruker software) and from Meisser et al. (1999) for strontiomelane. The name of the sample is indicated in the upper right corner. (a) Sr-rich Mn oxide diffracting as cryptomelane rather than strontiomelane (see Section 8); (b) hollandite; (c) romanechite mixed with goethite (G); (d) hollandite mixed with romanechite in a goethite (G) matrix; (e) hollandite and coronadite, not easily distinguishable, in a goethite (G) + quartz (Q) matrix; and (f) chalcophanite.

coronadite (CP04/20 cc) and a chalcophanite (CP04/43 cc). These samples, that represent the dominant Mn-bearing mineral phases in Tamra, were selected for their homogeneity thanks to binocular observation, ESEM and XRD investigations. Sample ZM1cc2 was however rejected due to a major atmospheric Ar contamination during analysis.

As a consequence, three Mn-oxide samples (ZM2cc2, CP04/20 cc and CP04/43 cc) were selected and analyzed by continuous laser probe (CO_2 Synrad®) step-wise heating ^{39}Ar–^{40}Ar technique. Millimetre-wide fragments of Mn oxides were wrapped in Al foil to form packets (11 mm × 11 mm × 0.5 mm). These packets were stacked up together with intercalated (every 10 samples) packets filled with flux monitors to form a pile. The stack, put in an irradiation can, was irradiated for 13.33 h (resulting in an integrated power of 40 MWH) in the 5C location of the McMaster reactor (Hamilton, Canada), with a total flux of 1.2×10^{18} n.cm^{-2}. The irradiation standard used is the TCR-2 sanidine, with an age of 28.34 ± 0.28 Ma relative to the primary biotite standard GA-1550, according to Renne et al. (1998).The alternative age (27.87 Ma), recently used by Calvert et al. (2006), would not, in this specific case, change significantly the calculated age. The sample arrangement allowed us to monitor the flux gradient with a precision of ±0.2%. The step-heating experimental procedure has been described in detail by Ruffet et al. (1995, 1997). Blanks are performed routinely each first or third run, and are subtracted from the subsequent sample gas fractions. Analyses are performed on a Map215® mass spectrometer. Our results yield a plateau age whenever, a minimum of three consecutive steps account for a corresponding minimum of at least 70% of the total $^{39}Ar_K$ released, and when individual fraction ages agree within 1 or 2σ with the integrated age of the plateau segment. All discussed ^{40}Ar–^{39}Ar results are displayed at the 1σ level.

Table 3
Major element contents within the minerals/mineral assemblages in each paragenetic stage in the MZD (semi-quantitative analyses using ESEM EDS probe). Fe content is quoted as FeO. XRD analyses of the minerals/mineral assemblages are also mentioned: G: goethite, C: coronadite, Ch: chalcophanite, Am.: amorphous Pb–Mn oxide, Cr: Sr-cryptomelane. Ar age is listed for sample CP04/20 cc.

Wt%	Distal Manganese Zone (MZD)																		
	Fe soft matrix (stage 1)			Fe-concretions (stage 2)				Mn–concretions											
								Ba–Sr–K-enriched (stage 3)		Pb–Zn-enriched (stage 4)									
Sample	CP 04/43	CP 04/32	CP 04/43 geod	CP 04/43 geod	CP 04/20 geod	CP 04/20 geod	CP 04/20 geod	CP 04/20 cc	CP 04/20 cc	CP 04/20 cc	CP 04/20 cc	CP 04/43 cc	CP 04/33	CP 04/32 geod	CP 04/32 geod	CP 04/32 geod	CP 04/43 cc	CP 04/43 cc	CP 04/43 cc
Analysis	C43–1	C32–1	C43–2	C43–3	C20–1	C20–2	C20–3	C20–4	C20–5	C20–6	C20–7	C43–4	C33–1	C32–2	C32–3	C32–4	C43–5	C43–6	C43–7
FeO	90.2	56.1	46.5	63.0	58.4	58.0	50.0	0.0	10.6	8.4	18.4	8.0	8.0	0.0	0.0	13.5	7.8	5.3	10.5
MnO	1.0	6.1	37.2	18.7	23.3	26.9	34.0	86.6	76.6	58.9	54.5	64.6	56.6	41.5	55.6	47.9	61.5	67.2	56.1
PbO	0.0	1.9	14.6	3.7	4.3	4.4	4.8	2.4	2.5	26.1	20.1	25.6	29.0	22.1	25.4	22.1	22.7	8.3	30.5
ZnO	3.8	0.0	1.7	8.9	9.7	5.9	5.5	3.8	3.2	3.0	3.9	1.7	2.4	0.0	0.0	0.0	6.1	19.2	3.0
SiO_2	5.0	19.0	0.0	0.0	3.6	2.8	3.6	0.0	0.7	0.8	0.9	0.0	1.2	19.1	9.6	8.3	0.0	0.0	0.0
Al_2O_3	0.0	17.0	0.0	2.5	2.8	2.1	1.5	0.8	0.9	0.9	0.8	0.0	2.8	17.2	9.3	8.2	0.6	0.0	0.0
SrO	0.0	0.0	0.0	1.2	0.0	0.0	0.0	4.7	4.4	1.4	1.0	0.0	0.0	0.0	0.0	0.0	1.3	0.0	0.0
BaO	0.0	0.0	0.0	0.0	0.0	0.0	0.0	0.0	0.0	0.0	0.0	0.0	0.0	0.0	0.0	0.0	0.0	0.0	0.0
K_2O	0.0	0.0	0.0	0.0	0.0	0.0	0.6	1.7	1.0	0.5	0.3	0.0	0.0	0.0	0.0	0.0	0.0	0.0	0.0
sum	100.0	100.0	100.0	100.0	100.0	100.0	100.0	100.0	100.0	100.0	100.0	100.0	100.0	100.0	100.0	100.0	100.0	100.0	100.0
BaO + SrO + K_2O	0.0	0.0	0.0	1.2	0.0	0.0	0.6	6.4	5.4	1.9	1.3	0.0	0.0	0.0	0.0	0.0	1.3	0.0	0.0
PbO + ZnO	3.8	1.9	16.3	12.5	14.0	10.2	10.3	6.2	5.7	29.2	24.1	27.3	31.3	22.1	25.4	22.1	28.8	27.5	33.5
DRX	G	G	G	G	G	G	G	Cr	Cr	C	C	C	C	Am.	Am.	Am.	C	Ch	C
^{39}Ar–^{40}Ar ages										3.35 ± 0.07 Ma							Too high atmospheric contamination		

Table 4
Major element contents within the minerals/mineral assemblages in each paragenetic stage in the MZP (semi-quantitative analyses using ESEM EDS probe). Fe content is quoted as FeO. XRD analyses of the minerals/mineral assemblages are also mentioned: G: goethite, C: coronadite, Ch: chalcophanite, Cr: Sr-cryptomelane, R: romanechite, H: hollandite. Ar age is listed for sample ZM2cc2.

Wt%	Proximal Manganese Zone (MZP)													
	Fe soft matrix (stage 1)		Fe-concretions (stage 2)				Mn-concretions							
							Ba–Sr–K-enriched (stage 3)					Pb–Zn-enriched (stage 4)		
Sample	ZM1	ZM1	ZM1	ZM1	ZM2cc1	ZM2cc1	ZM1cc2	ZM2cc2	ZM2cc2	ZM1cc1	ZM2cc2	ZM2cc2	ZM2cc2	ZM1cc2
Analysis	ZM1–1	ZM1–2	ZM1–3	ZM1–4	ZM2–1	ZM2–2	ZM1–5	ZM2–3	ZM2–4	ZM1–6	ZM2–5	ZM2–6	ZM2–7	ZM1–7
FeO	88.9	84.3	48.0	42.9	65.1	50.1	8.8	0.0	13.2	20.1	16.0	13.2	12.5	17.4
MnO	1.6	5.7	35.9	39.1	17.8	31.3	73.7	81.6	73.0	60.5	72.6	57.0	65.7	57.3
PbO	0.0	0.0	0.0	2.0	4.8	5.8	4.3	2.7	3.6	3.8	3.0	23.0	15.7	0.0
ZnO	3.5	4.8	11.8	11.7	6.6	6.1	3.1	4.2	3.7	9.3	3.7	3.3	3.1	21.1
SiO_2	4.1	2.4	2.9	1.6	4.1	1.5	0.4	0.3	0.0	0.7	0.7	0.0	0.0	0.6
Al_2O_3	1.9	0.8	1.0	1.1	1.6	2.1	0.8	0.7	0.0	0.6	0.5	0.0	0.4	0.5
SrO	0.0	2.0	0.0	1.2	0.0	1.3	1.9	4.0	1.6	1.4	2.7	1.9	2.1	2.1
BaO	0.0	0.0	0.0	0.0	0.0	1.9	5.8	5.6	4.2	2.7	0.0	1.6	0.0	0.7
K_2O	0.0	0.0	0.4	0.5	0.0	0.0	1.2	0.8	0.7	0.9	0.8	0.0	0.5	0.4
Sum	100.0	100.0	100.0	100.0	100.0	100.0	100.0	100.0	100.0	100.0	100.0	100.0	100.0	100.0
BaO + SrO + K_2O	0.0	2.0	0.4	1.8	0.0	3.2	8.9	10.4	6.5	5.0	3.5	3.5	2.5	3.2
PbO + ZnO	3.5	4.8	11.8	13.7	11.4	11.9	7.4	6.9	7.3	13.1	6.7	26.3	18.8	21.1
DRX	G	G	G	G	G	G	R	H	H	R	Cr	C	C	Ch
^{39}Ar–^{40}Ar ages								4.7 ± 0.1 Ma		Major atmospheric Ar contamination during analysis				

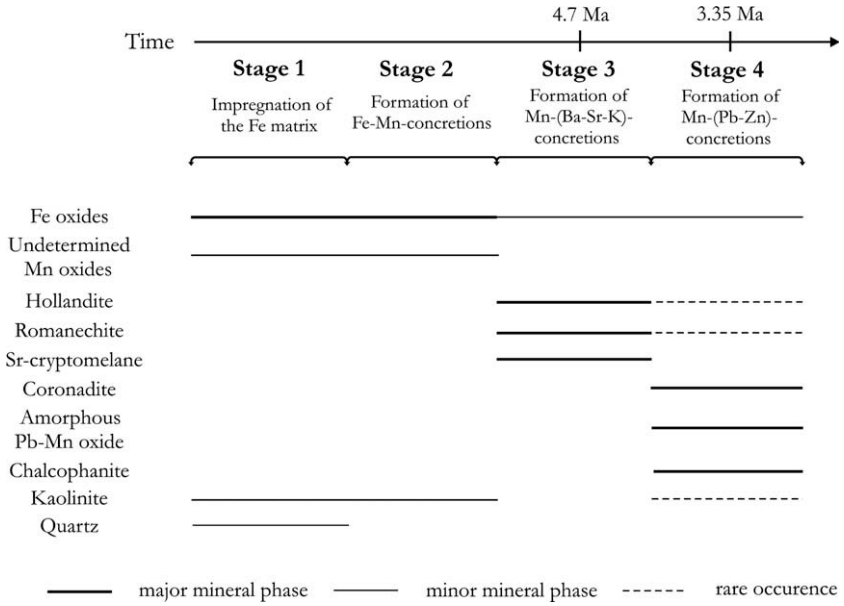

Fig. 4. Synthetic paragenetic sequence of the mineral phases in the Tamra Fe–Mn deposit. Solid lines represent the distribution of major minerals while dashed lines are for minerals having a local occurrence. "Undetermined Mn oxides" correspond to Mn oxides intimately mixed with a ferruginous matrix, for which no distinctive XRD pattern has been obtained. ^{39}Ar–^{40}Ar ages were those obtained for this study.

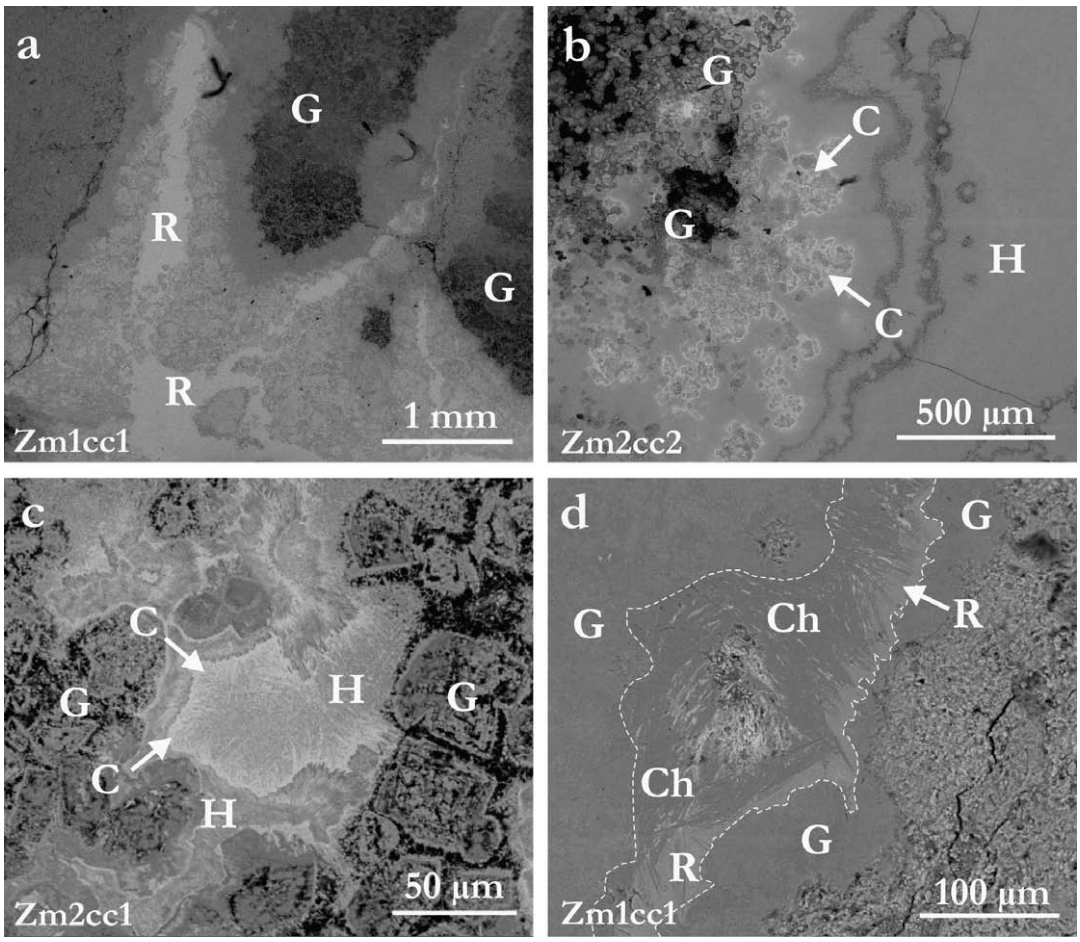

Fig. 5. ESEM micrographs (backscattered electrons) of the Mn-bearing mineralizations in the MZP. "G", "R", "H", "C" and "Ch" are respectively for goethite, romanechite, hollandite, coronadite and chalcophanite. The name of the sample is indicated in the lower left corner. (a) Romanechite fissure fillings within a goethitic concretion: there is a gradient to heavier Mn enrichment toward the centre of the fissure; medium grey shades are for romanechite + goethite mixing, while romanechite (light grey) is observed in the centre of the fissure. (b) Massive hollandite concretion surrounding goethite grains or grain aggregates. The edge between goethite and hollandite is underlined by a thin bright coronadite rim. (c) Alternating growing of hollandite and coronadite as needles (or needle bundles) within goethite voids. (d) Complex fissure filling (delineated by dashed lines) within a goethite concretion, consisting of interpenetrated chalcophanite needles and romanechite.

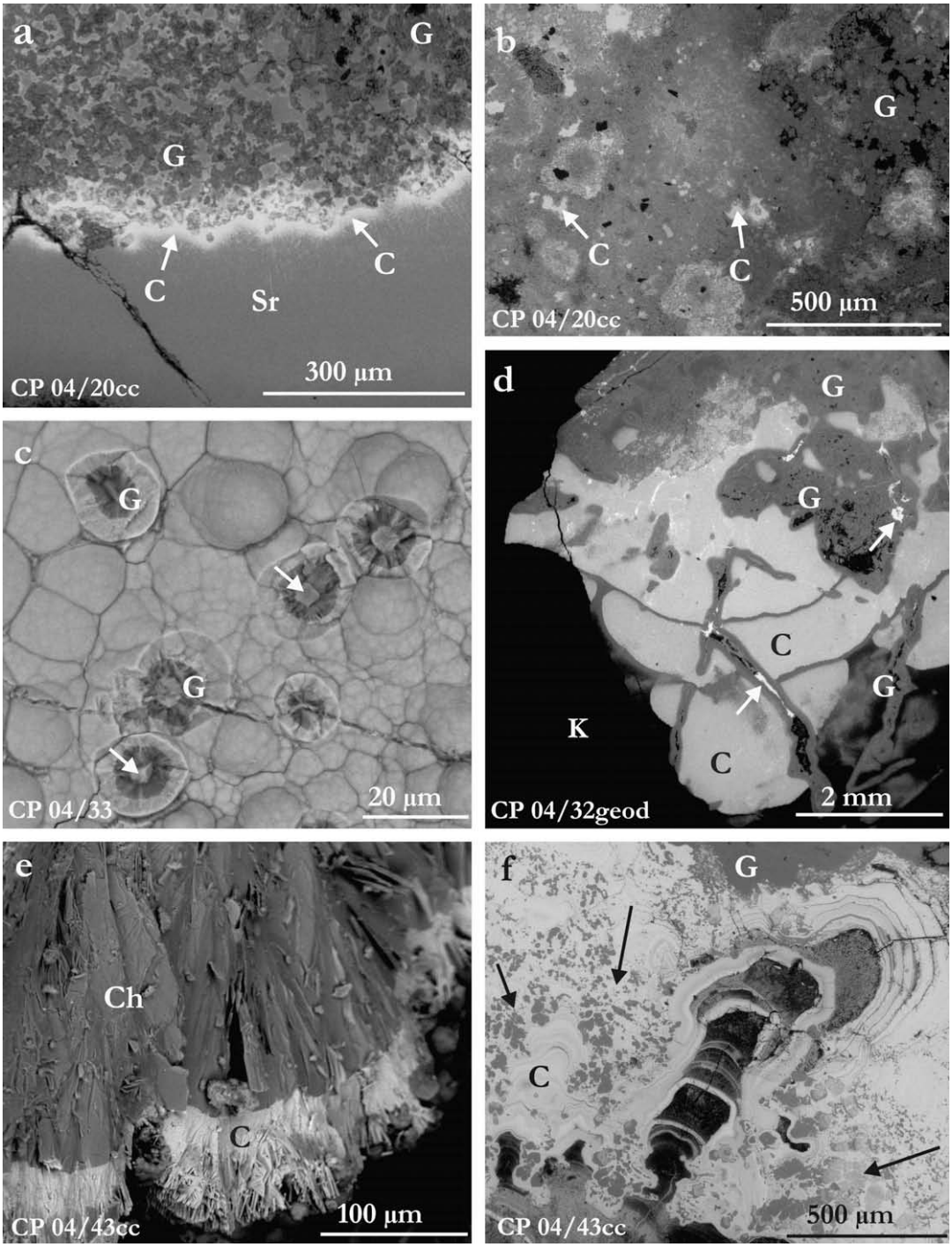

Fig. 6. ESEM micrographs (backscattered electrons) of the Mn-bearing mineralizations in the MZD. "G", "Sr", "C", "Ch" and "K" are for goethite, Sr-cryptomelane, coronadite, chalcophanite and kaolinite, respectively. The name of the sample is indicated in the lower left corner. (a) Sr-cryptomelane surrounding goethite grains (upper part of the micrograph), and massive Sr-cryptomelane concretions (lower part of the micrograph) enclosing larger goethite–Sr-cryptomelane plates. The edge between these plates and the massive Sr-cryptomelane is underlined by a bright coronadite needle rim. (b) Coronadite filling tubes and voids within mixed Fe–Mn concretion. (c) Concentric array of mineral phases within tubules feeding mammillated coronadite (see micrograph d): the Pb–Mn oxide core (white arrows) is surrounded by Fe oxides and then by a final lining of Pb–Mn oxide. (d) Mammillated amorphous Pb–Mn oxide growing in contact with a kaolinite layer. Iron oxides underline each Pb–Mn oxide crystallization episode and partially fill late-formed contorted tube-like cavities crosscutting the Pb–Mn oxide drops and the adjacent kaolinite horizon. White arrows show the later infillings made up from patches of Pb–Mn oxide mixed with Fe oxides. (e) Needle-like crystallizations (up to 70 µm) of coronadite in apical position with regard to the chalcophanite fan-like flakes. (f) Coronadite concretions alternating with cauliflower textured iron oxides that are regarded as stromatolitic in origin. Arrows show several growing directions of ferruginous stromatolites.

7.1. Dating hollandite and coronadite

Hollandite and coronadite pertain to the hollandite group (Post, 1999). Hollandite group minerals are regarded as suitable minerals for ^{39}Ar–^{40}Ar dating of weathering events due to: (1) its relative abundance as monominerals in weathering profiles, (2) its capacity to retain potassium after crystallization in tunnels within its structure, and (3) its capacity to retain argon in these tunnels (Vasconcelos, 1999). Previous investigations suggest that fine-scale, laser-probe ^{39}Ar–^{40}Ar technique is most appropriate for

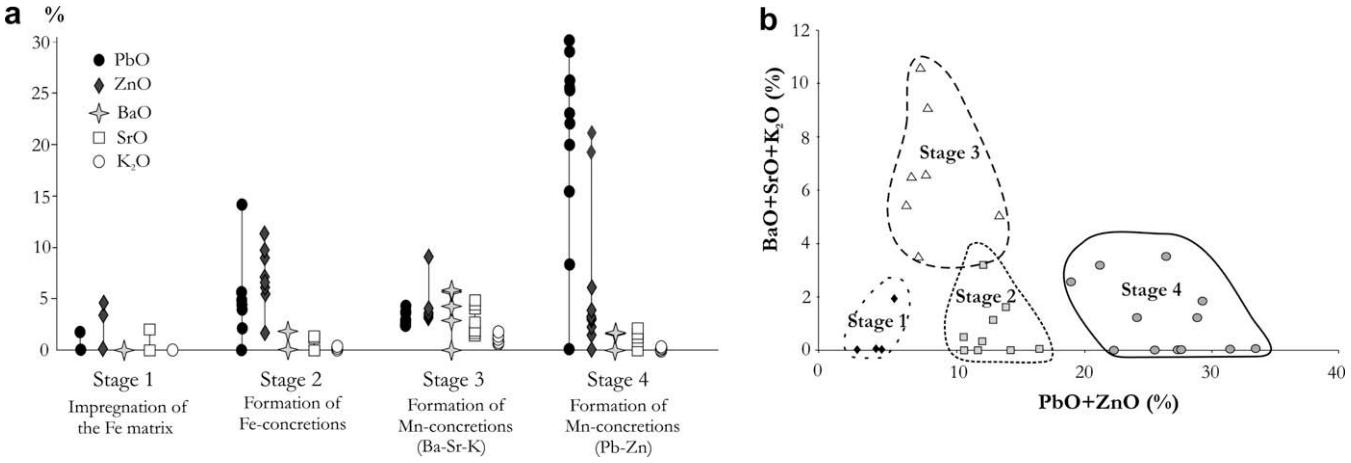

Fig. 7. Geochemical evolution of Mn oxide deposits: (a) Comparison of PbO, ZnO, BaO, SrO and K_2O contents in several minerals or mineral assemblages for each paragenetic stage. (b) Evolution of BaO + SrO + K_2O and PbO + ZnO contents for each paragenetic stage.

dating weathering phenomena, since it allows the detection of contaminating phases and of multiple generations of weathering minerals (Vasconcelos et al., 1994; Ruffet et al., 1996; Hénocque et al., 1998). The similarity in the properties of hollandite $(Ba,K)_{0.8\text{-}1.5}Mn_8O_{16}\cdot nH_2O$ and coronadite $(Pb,Ba,K)_{0.8\text{-}1.5}Mn_8O_{16}\cdot nH_2O$ suggests that coronadite is also suitable for $^{40}Ar/^{39}Ar$ geochronology (Bish and Post, 1989; Vasconcelos, 1999). This study presents the first $^{39}Ar–^{40}Ar$ analyses of coronadite.

Sample ZM2cc2 is an homogeneous hollandite ($^{37}Ar_{Ca}/^{39}Ar_K$ ratio nearly constant, Fig. 8a) from stage 3 that displays a rather low level of atmospheric contamination (down to 74.4%, Table 5) in the intermediate temperature steps; it yields a rather flat age spectrum allowing plateau age calculation at 4.7 ± 0.1 Ma (Fig. 8b).

Sample CP04/20 cc is comprised of dominant stage 4 coronadite with very minor hollandite, present as needles within coronadite (as confirmed by ESEM examination). As shown in Fig. 8a, the homogeneity of the sample in steps 4–8, where the plateau age is calculated, is however good ($^{37}Ar_{Ca}/^{39}Ar_K$ ratio nearly constant). It is less contaminated by atmospheric argon ($^{40}Ar_{atm}$ down to 58.6%, Table 5) and displays a very flat age spectrum over ca 86% of $^{39}Ar_K$ degassing allowing a plateau age calculation at 3.35 ± 0.07 Ma (Fig. 8b). Both experiments yield isochron age calculations highly concordant with corresponding plateau ages. Their $(^{40}Ar/^{36}Ar)_i$ intercepts are indistinguishable of atmospheric ratio.

7.2. Dating chalcophanite

Chalcophanite $(Zn,Fe^{2+},Mn^{2+})Mn_3^{4+}O_7\cdot 3(H_2O)$ is also a common weathering product in many Mn-bearing base metal deposit (Post, 1999). However, chalcophanite has a low K-content and shows a crystalline layer structure, with sheets of edge-sharing $Mn(IV)O_6$ octahedra that alternate with layers of Zn cations and water molecules (Post, 1999).

Sample CP04/43 cc is an homogeneous chalcophanite from paragenetic stage 4, which unfortunately is marked by a very high atmospheric contamination (99.9% down to 96.8% at fusion step) and a very low K-content (# $^{39}Ar_K$). It yields a poorly defined age spectrum with very large age error bars. Calculated plateau age at 6.6 ± 6.4 Ma is not significant. Isochron age, at 6.0 ± 1.3 Ma ($(^{40}Ar/^{36}Ar)_i$ = 295.6 ± 0.2), but with a very low MSWD of 0.07, is no more significant.

The "hollandite-type" retentive tunnels-structure is lacking. Together with low K-content, this should explain the absolute high atmospheric contamination (99.9% down to 96.8% at fusion step) and thus the poorly defined age spectrum with very large age error bars (calculated "plateau age" at 6.6 ± 6.4 Ma). Isochron age, at 6.0 ± 1.3 Ma ($(^{40}Ar/^{36}Ar)_i$ = 295.6 ± 0.2), is also not consistent with the observed succession of crystallization: chalcophanite crystallized at the end of stage 4, after hollandite (4.7 ± 0.1 Ma) and coronadite (3.35 ± 0.07 Ma). The very low MSWD of 0.07 shows that the isochron calculation is influenced by the very large errors. Although new analyses must be performed on chalcophanite from different contexts, this study suggests that this mineral is not suitable for $^{39}Ar–^{40}Ar$ dating.

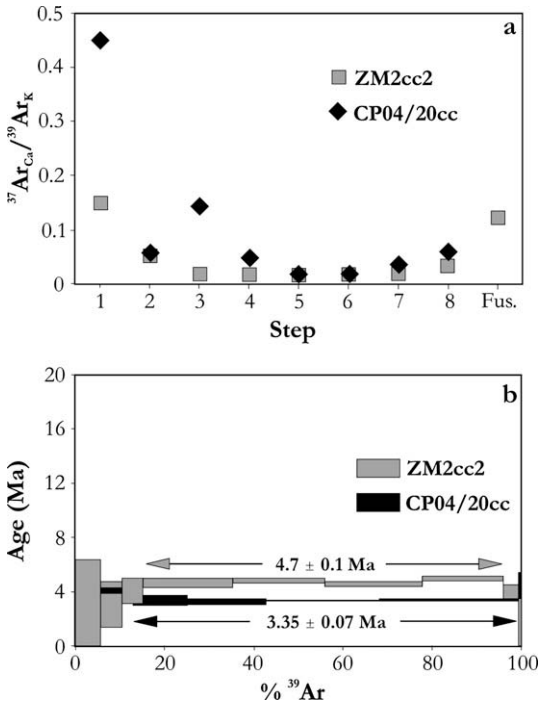

Fig. 8. (a) $^{37}Ar_{Ca}/^{39}Ar_K$ vs. step number plot, allowing checking the two samples homogeneity. (b) $^{39}Ar–^{40}Ar$ age plateau age calculations for the two samples ZM2cc2 and CP04/20 cc.

8. Discussion

8.1. Mineralization dating and geodynamic events

$^{39}Ar–^{40}Ar$ dating of hollandite-type manganese oxides yielded an accurate dating of minerals that are considered to have formed

Table 5
$^{40}Ar/^{39}Ar$ analytical data. $^{40}Ar_{atm}$ = atmospheric ^{40}Ar. $^{40}Ar^*$ = radiogenic ^{40}Ar. Ca = produced by Ca-neutron interferences. K = produced by K-neutron interferences. Age (Ma) = the date is calculated using the decay constants recommended by Steiger and Jäger (1977). The errors are at the 1 level and do not include the error in the value of the J parameter. Correction factors for interfering isotopes produced by neutron irradiation in the McMaster reactor are $(^{39}Ar/^{37}Ar)_{Ca} = 7.06 \times 10^{-4}$, $(^{36}Ar/^{37}Ar)_{Ca} = 2.79 \times 10^{-4}$, $(^{40}Ar/^{39}Ar)_K = 2.97 \times 10^{-2}$.

Step	$^{40}Ar_{Atm}$ (%)	$^{39}Ar_K$ (%)	$^{37}Ar_{Ca}/^{39}Ar_K$	$^{40}Ar^*/^{39}Ar_K$	Age (Ma)
ZM2cc2 Hollandite					
1	99.5	5.6	1.48E−01	0.28	2.6 ± 3.8
2	98.1	4.9	5.10E−02	0.33	3.1 ± 1.7
3	94.2	4.7	1.60E−02	0.43	4.1 ± 0.9
4	87.4	20.1	1.60E−02	0.49	4.7 ± 0.3
5	74.4	20.6	1.50E−02	0.51	4.8 ± 0.2
6	77.3	22.0	1.70E−02	0.48	4.6 ± 0.2
7	78.8	18.0	1.80E−02	0.53	5.0 ± 0.2
8	85.4	3.6	3.30E−02	0.41	3.9 ± 0.6
Fusion	98.9	0.6	1.23E−01	0.07	0.7 ± 3.8
CP04/20cc Coronadite (+Hollandite)					
1	86.4	5.5	4.48E−01	0.45	4.24 ± 0.65
2	74.7	5.6	4.80E−02	0.43	4.07 ± 0.20
3	80.8	1.9	1.42E−01	0.43	4.10 ± 0.46
4	91.9	12.1	5.00E−02	0.36	3.37 ± 0.37
5	82.1	17.7	1.70E−02	0.34	3.26 ± 0.18
6	58.6	25.3	1.70E−02	0.35	3.35 ± 0.05
7	59.7	19.7	3.40E−02	0.36	3.40 ± 0.08
8	60.0	11.4	5.90E−02	0.36	3.40 ± 0.08
9	74.1	0.7	–	0.46	4.34 ± 1.06
Fusion	94.8	0.2	–	1.27	12.04 ± 3.71
CP04/43cc Chalcophanite					
1	99.9	32.6	1.37E+01	1.35	12.7 ± 53.3
2	99.6	40.9	4.88E+00	0.58	5.5 ± 9.8
3	98.8	24.9	3.97E+00	0.77	7.2 ± 6.1
Fusion	96.8	1.6	1.66E+01	2.81	26.4 ± 46.7

in two different paragenetic stages: hollandite from stage 3 formed at 4.7 ± 0.1 Ma and coronadite from stage 4 formed at 3.35 ± 0.07 Ma. As suggested above, hollandite and associated mineral phases in stage 3 result from the input of a (Ba, Sr, K)-rich hydrothermal fluid within the Tamra sediments, in contrast with the stage 2 minerals that were preferentially enriched in Pb and Zn. In stage 3, a wider distribution throughout the entire MZ is noted for the more mobile elements, i.e. K and Sr, while Ba is mainly concentrated in the MZP, which is located in the immediate vicinity of the presumed Ba source (Sidi Driss ore deposit; Decrée et al., 2008b).

The most mobile elements from the Sidi Driss deposits could have been leached by stage 3 hydrothermal circulations; once leached, these elements migrated outward and upward according to their relative stability in the fluid phase: i.e. K ∼ Sr > Ba. This event probably corresponds to a late phase in the hydrothermal circulation system that was responsible for the deposition of the Messinian Sidi Driss ores. The Sidi Driss hydrothermal system has most probably been initiated in relation with the regional Upper Miocene magmatism (Decrée et al., 2008b). During the Pliocene, a weakening in the hydrothermal system allowed for increasing mixing between hydrothermal fluids and meteoric waters, the latter eventually predominating.

This mixing of hydrothermal and meteoric fluids induced the crystallization of the typical supergene phases such as hollandite, coronadite and chalcophanite.

The coronadite age, at 3.35 ± 0.07 Ma, records a significant Pb–Zn enrichment event corresponding to a new pulse of leaching of the underlying Sidi Driss ore deposits, and to the subsequent input of the mobilized metals within the Tamra sediments. Unlike earlier mineralizing events (stage 2 and 3), this late one cannot be connected anymore with the Messinian magmatic activity. The geodynamic evolution and its consequences (i.e. high thermal gradient and enhanced metal mobilization, including Fe, Pb, Zn), is marked in the field by: (i) the occurrence of N–S subvertical, normal faults crosscutting the whole Tamra series (and thus postdating it) and (ii) the emplacement within these fractures of a Pb–Zn–Fe paragenesis (galena, sphalerite and pyrite).

These late normal faults cross-cutting the Tamra series suggest that the area experienced late extensional events, at/around 3.35 Ma, which are part of the complex succession of Neogene compressional/extensional episodes relating to the Africa-Eurasia convergence (Bouaziz et al., 2002). This extension and its possible associated increased thermal gradient, have most probably reactivated convection cells, and the hydrothermal leaching of the regional substrate. Elements carried through these late circulations could contribute to the MZ mineralization (as suggested by Pb isotopes, unpublished data).

8.2. Mineralization and pollutant trapping in the Tamra mine

Around the Tamra mine, despite: (i) the great amount of elements trapped in the Tamra iron ore, (ii) the present-day high thermal gradient and (iii) the polyphased mineralization events, the Fe, Pb, Zn and Mn contents within present day local springs are several orders of magnitude lower than the WHO standards for natural drinking waters.

Ages obtained on mineralization stages 3 and 4 suggest that the major part of the Fe, Pb, Zn and Mn stock was efficiently and durably trapped within the Tamra sediments as mixed Mn oxides (e.g. coronadite, chalcophanite and hollandite). The efficient metal trapping mechanism took place soon after the influx of hydrothermal fluids in the waterlogged Tamra sediments. Indeed, such a process would account for the mixing between tepid, reduced and acid (hydrothermal) fluids and subsurface meteoric-derived fluids. This process has most probably played a significant role in hampering any subsequent massive dispersion of elements (Fe, Pb, Zn and Mn) in the sediments farther than the MZ.

Another part of the potential pollutant stock is trapped within the soft ferruginous matrix or in the mixed Fe–Mn concretions/boxworks. The association of Fe and Mn oxides, both being characterized by high specific surfaces, is known to efficiently trap heavy metals as coatings (adsorbed complex) or co-precipitates (Balistrieri and Murray, 1986; Manceau et al., 1992; Dong et al., 2000; O'Reilly and Hochella, 2003; Bradl, 2004; Feng et al., 2007). The efficient trapping of heavy metals within mineral phases (as constituting elements) and/or their adsorption onto Fe and Mn oxides both account for the drinkable character of the present day springs. Colloidal and/or any other labile/mobile Fe, Mn phases are especially low in the present-day fluids, probably because they are themselves likely to be efficiently trapped on pre-existing Fe and Mn oxides. Similarly, lead is prone to be strongly adsorbed onto manganese oxides (Hettiarachchi et al., 2000; Bradl, 2004) and more particularly onto biogenic ones (Dong et al., 2000, 2003; Villalobos et al., 2005 and references therein; Bargar et al., 2009). Part of the Mn oxides from the MZ is obviously biogenic in origin, as suggested by intergrowth with microstromatolitic Fe oxides (as observed in Fig. 6f).

Contrary to Pb, Zn is known to be one of the less efficiently adsorbed heavy metals in soils (Fontes and Gomes, 2003); it is therefore not surprising that Zn actually is one of the most concentrated elements in our present-day fluids.

On the other hand, the abundance of Sr and Ba in fluids might result from three distinct and/or coexisting mechanisms:

(1) more intense leaching of hollandite, romanechite and Sr-cryptomelane relative to coronadite;
(2) similar leaching rate of all these mineral phases but with better retention of Pb on soils/sediments; and

(3) deep circulation allowing the mixing between Sidi Driss fluids and meteoric circulation resurging in Tamra.

Mechanism (3) is supported by the similarity between fluid compositions in Tamra and in the immediate vicinity of Sidi Driss, especially by the Sr > Zn > Ba > Pb contents, but the intervention of the other two mechanisms cannot be ruled out.

9. Conclusions

Textural, geochemical and isotopic analyses of manganiferous deposits in the Tamra mine have emphasized the complex and polyphase nature of these mineralizations. Four stages were defined using Mn oxide speciation and Fe oxide facies/textures. The first two stages relate to the pedogenetic event in the Tamra series that gave rise to the economic Fe deposit and to a Fe and Mn reconcentration in the form of oxide concretions occurring within the soft ferruginous sediment. The last two stages (i.e. stages 3 and 4) relate to mineralizing events linked to later hydrothermal circulations that could have leached the Sidi Driss ore and/or other sources in the regional substrate. Stage 3 at 4.7 ± 0.1 Ma records the input of Ba, Sr and K within the Tamra sediments, resulting in the formation of massive romanechite, hollandite and Sr-cryptomelane. Stage 4 at 3.35 ± 0.07 Ma is characterized by high Pb and Zn influx and subsequent formation of coronadite and chalcophanite. This episode is relating to the Late Miocene extensional event, which obviously lasted into the Zanclean–Piacenzian boundary in the studied area. Our study moreover suggests that chalcophanite is not suitable for ^{39}Ar–^{40}Ar dating.

From an environmental viewpoint, the efficient trapping of metals as mixed and complex Mn oxides (e.g. coronadite and chalcophanite) soon after they were brought within the Tamra sediments – as demonstrated by the ^{39}Ar–^{40}Ar ages – has significantly hampered their migration around the mine or within the resurging fluids that are an everyday source of drinking waters for local population.

Acknowledgements

The first author (SD) thanks the Belgian Fund for Scientific Research (FNRS), for providing her with a FRIA PhD Grant. Fieldwork in spring 2004 was founded by a NATO linkage Grant dedicated to the study of "Special clays in Northern Tunisia" (ref 980498). Jean-Paul Liégeois is also thanked for his helpful comments. Ch. Marignac and an anonymous reviewer are warmly thanked for their constructive comments.

References

Appelo, C., Postma, D., 1994. Geochemistry, Groundwater and Pollution. Balkema Ed, Rotterdam.

Balistrieri, L.S., Murray, J.W., 1986. The surface chemistry of sediments from the Panama Basin: the influence of Mn oxides on metal adsorption. Geochimica et Cosmochimica Acta 50, 2235–2243.

Bargar, J.R., Fuller, Ch.C., Marcus, M.A., Brearley, A.J., De la Rosa, M.P., Webb, S.M., Caldwell, W.A., 2009. Structural characterization of terrestrial microbial Mn oxides from Pinal Creek. AZ.Geochimica et Cosmochimica Acta 73, 889–910.

Beauvais, A., Ruffet, G., Colin, F., Hénocque, O., 2008. ^{39}Ar–^{40}Ar dating of supergene K–Mn oxides, weathering and erosion rhythms of the West African Cenozoic morphogenesis. Journal of Geophysical Research – Earth Surface 113, F04007. doi:10.1029/2008JF000996.

Bish, D.L., Post, J.E., 1989. Thermal behaviour of complex, tunnel-structure manganese oxides. American Mineralogist 74, 177–186.

Bouaziz, S., Barrier, E., Soussi, M., Turki, M.M., Zouari, H., 2002. Tectonic evolution of the northern African margin in Tunisia from paleostress data and sedimentary record. Tectonophysics 357, 227–253.

Bouchard, M., Laforest, F., Vandelac, L., Bellinger, D., Mergler, D., 2007. Children and hyperactive behaviors: pilot study of school-age children exposed through tap water. Environmental Health Perspectives 115, 122–127.

Boulvain, F., 1989. Origine microbienne du pigment ferrugineux des monticules micritiques du Frasnien de l'Ardenne. Annales Société Géologique de Belgique 112, 79–85.

Bouzouada, R., 1992. Géologie, minéralogie et paragenèses des gites de fer du District des Nefza. Répartition des sulfures et des impuretés. DEA thesis, Tunis II University, 77p.

Bradl, H.B., 2004. Adsorption of heavy metal ions on soils and soils constituents. Journal of Colloid and Interface Science 277, 1–18.

Calvert, A.T., Moore, R.B., McGeehin, J.P., Rodrigues da Silva, A.M., 2006. Volcanic history and $^{40}Ar/^{39}Ar$ and ^{14}C geochronology of Terceira Island, Azores, Portugal.

Chan, M.A., Parry, W.T., Petersen, E.U., Hall, C.M., 2001. $^{40}Ar/^{39}Ar$ age and chemistry of manganese mineralization in the Moab and Lisbon fault systems, southeastern Utah. Geology 29, 331–334.

Colin, F., Beauvais, A., Ruffet, G., Hénocque, O., 2005. First $^{40}Ar/^{39}Ar$ geochronology of lateritic manganiferous pisolites: implications for the Palaeogene history of a West African landscape. Earth and Planetary Sciences Letters 238, 172–188.

Dammer, D., McDougall, I., Chivas, A.R., 1999. Timing of weathering-induced alteration of manganese deposits in Western Australia: evidence from K–Ar and ^{40}Ar–^{39}Ar dating. Economic Geology 94, 87–108.

Decrée, S., De Putter, Th., Yans, J., Recourt, Ph., Jamoussi, F., Bruyère, D., Dupuis, Ch., 2008a. Iron mineralization in Pliocene sediments of the Tamra iron mine (Nefza mining district, Tunisia): mixed influence of pedogenesis and hydrothermal alteration. Ore Geology Reviews 33, 397–410.

Decrée, S., Marignac, Ch., De Putter, Th., Deloule, E., Liégeois, J.-.P., Demaiffe, D., 2008b. Pb–Zn mineralizations in a Miocene regional extensional context: the case of the Sidi Driss and the Douahria ore deposits (Nefza mining district, N. Tunisia). Ore Geology Reviews 34, 285–303.

Dermech, M., 1990. Le complexe de l'Oued Bélif – Sidi Driss (Tunisie septentrionale). Hydrothermalisme et métallogénie. Unpublished PhD thesis, Paris VI University, 336p.

Dong, D., Nelson, Y.M., Lion, L.W., Shuler, M.L., Ghiorse, W.C., 2000. Adsorption of Pb and Cd onto metal oxides and organic material in natural surface coatings as determined by selective extractions: new evidence for the importance of Mn and Fe oxides. Water Research 34, 427–436.

Dong, D., Derry, L.A., Lion, L.W., 2003. Pb scavenging from a freshwater lake by Mn oxides in heterogeneous surface coating materials. Water Research 37, 1662–1666.

Ehrlich, H.L., 2002. Geomicrobiology. Marcel Dekker, New York.

Feng, X.H., Zhai, L.M., Tan, W.F., Liu, F., He, J.Z., 2007. Adsorption and redox reactions of heavy metals on synthesized Mn oxide minerals. Environmental Pollution 147, 366–373.

Flügel, E., 2004. Microfacies of carbonate rocks. Analysis, interpretation and application. Springer-Verlag, Berlin. 768p..

Fontes, M., Gomes, P., 2003. Simultaneous competitive adsorption of heavy metals by the mineral matrix of tropical soils. Applied Geochemistry 18, 795–804.

Hautmann, S., Lippolt, H.J., 2000. ^{40}Ar–^{39}Ar dating of central European K–Mn oxides – a chronological framework of supergene alteration processes during the Neogene. Chemical Geology 170, 37–80.

Hénocque, O., Ruffet, G., Colin, F., Féraud, G., 1998. $^{40}Ar/^{39}Ar$ dating of West African lateritic cryptomelanes. Geochimica et Cosmochimica Acta 62, 2739–2756.

Hettiarachchi, G., Pierzynski, P., Ransom, M., 2000. In situ stabilization of soil lead using phosphorus and manganese oxide. Environmental Science and Technology 34, 4614–4619.

Jallouli, C., Inoubli, M.H., Albouy, Y.Y., 1996. Le corps igné de Nefza (Tunisie septentrionale): caractéristiques géophysiques et discussion du mécanisme de sa mise en place. Notes du service Géologique de Tunisie N 62, 109–123.

Li, J.-.W., Vasconcelos, P., 2002. Cenozoic continental weathering and its implications for the palaeoclimate: evidence from $^{40}Ar/^{39}Ar$ geochronology of supergene K–Mn oxides in Mt Tabor, central Queensland, Australia. EPSL 200, 223–239.

Li, J.W., Vasconcelos, P., Duzgoren-Aydin, N., Yan, D.-.R., Zhang, W., Deng, D.D., Zhao, X.F., Zeng, Z.P., Hu, M.A., 2007. Neogene weathering and supergene manganese enrichment in subtropical South China. An $^{40}Ar/^{39}Ar$ approach and paleoclimatic significance. EPSL 256, 389–402.

Manceau, A., Charlet, L., Boisset, M.C., Didier, B., Spadini, L., 1992. Sorption and speciation of heavy metals on hydrous Fe and Mn oxides. From microscopic to macroscopic. Applied Clay Science 7, 201–223.

Meisser, N., Perseil, E.-.A., Brugger, J., Chiappero, P.-.J., 1999. Strontiomelane, Sr(Mn4+)6(Mn3+)2(O16), a new mineral species of the cryptomelane group from St. Marcel-Praborna, Aosta Valley, Italy. The Canadian Mineralogist 37, 673–678.

Mlayah, A., Ferreira da Silva, E., Rocha, F., Hamza, C.B., Charef, A., Noronha, F., 2009. The Oued Mellègue: mining activity, stream sediments and dispersion of base metals in natural environments, North-western Tunisia. Journal of Geochemical Exploration 102, 27–36.

Mote, T.I., Becker, T.A., Renne, P., Brimhall, G.H., 2001. Chronology of exotic mineralization at El Salvador, Chile, by $^{40}Ar/^{39}Ar$ dating of copper wad and supergene alunite. Economic Geology 96, 351–366.

Naddeo, V., Zarra, T., Belgiorno, V., 2008. A comparative approach to the variation of natural elements in Italian bottled waters according to the national and international standard limits. Journal of Food Composition and Analysis 21, 505–514.

Negra, L., 1987. Pétrologie, minéralogie et géochimie des minéralisations et des roches encaissantes des basins associés aux structures tectoniques et magmatiques de l'Oued Bélif et du Jebel Haddada (Nord des Nefza, Tunisie septentrionale). Unpublished PhD thesis, Paris-Sud university, 223p.

O'Reilly, S.E., Hochella Jr., M.F., 2003. Lead sorption efficiencies of natural and synthetic Mn and Fe-oxides. Geochimica et Cosmochimica Acta 67, 4471–4487.
Post, J.E., 1999. Manganese oxide minerals: crystal structures and economic and environmental significance. Proceedings of the National Academy of Science 96, 3447–3454.
Renne, P.R., Swisher, C.C., Deino, A.L., Karner, D.B., Owens, T.L., DePaolo, D.J., 1998. Intercalibration of standards, absolute ages and uncertainties in $^{40}Ar/^{39}Ar$ dating. Chemical Geology 145, 117–152.
Rouvier, H., 1977. Géologie de l'extrême Nord-Tunisien: tectoniques et paléogéographie superposées à l'extrémité orientale de la chaîne Nord-Maghrebine. Unpubl. PhD thesis Pierre et Marie Curie Univ., Paris, France, 215p.
Rouvier, H., Perthuisot, V., Mansouri, A., 1985. Pb–Zn deposits and salt-bearing diapirs in Southern Europe and North Africa. Economic Geology 80, 666–687.
Ruffet, G., Féraud, G., Ballèvre, M., Kiénast, J.-.R., 1995. Plateau ages and excess argon in phengites: an ^{40}Ar–^{39}Ar laser probe study of Alpine micas (Sesia Zone, Western Alps, northern Italy). Chemical Geology (Isotopic Geoscience Section) 121, 327–343.
Ruffet, G., Innocent, C., Michard, A., Féraud, G., Beauvais, A., Nahon, D., Hamelin, B., 1996. A geochronological $^{40}Ar/^{39}Ar$ and $^{87}Rb/^{86}Sr$ study of K–Mn oxides from the weathering sequence of Azul, Brazil. Geochimica et Cosmochimica Acta 60, 2219–2232.
Ruffet, G., Gruau, G., Ballèvre, M., Féraud, G., Philippot, P., 1997. Rb–Sr and ^{40}Ar–^{39}Ar laser probe dating of high-pressure phengites from the Sesia zone (western Alps): underscoring of excess argon and new age constraints on the high-pressure metamorphism. Chemical Geology 141, 1–18.
Schreyer, W., Fransolet, A.-.M., Bernhardt, H.-J., 2001. Hollandite–strontiomelane solid solutions coexisting with kanonaite and braunite in late quartz veins of the Stavelot Massif, Ardennes, Belgium. Contributions to Mineralogy and Petrology 141, 560–571.
Spier, C.A., Vasconcelos, P.M., Oliveira, S.M.B., 2006. $^{40}Ar/^{39}Ar$ geochronological contraints on the evolution of lateritic iron deposits in the Quadrilatero Ferrifero, Minas Gerais, Brazil. Chemical Geology 234, 79–104.
Stambouli-Essassi, S., Roche, E., Bouzid, S., 2007. Evolution de la végétation et du climat dans le Nord-ouest de la Tunisie au cours des 40 derniers millénaires. Geo-Eco-Trop 31, 171–214.
Stefanov, St. Hr., Ouchev, A., 1972. Gisement plombo-zincifère de Sidi Driss. Rapport géol.avec estimation de réserves. Rapport interne, Office National des Mines de Tunisie.
Steiger, R.H., Jäger, E., 1977. Subcommission on geochronology: convention on the use of decay constants in geo- and cosmochronology. Earth and Planetary Science Letters 36, 359–362.
Stumm, W., Morgan, J.J., 1996. Aquatic Chemistry. Wiley, New York.
Vasconcelos, P.M., 1999. K–Ar and ^{40}Ar–^{39}Ar geochronology of weathering processes. Annual Review of Earth and Planetary Sciences 27, 183–229.
Vasconcelos, P.M., Becker, T.A., Renne, P.R., Brimhall, G.H., 1992. Age and duration of weathering by ^{40}K–^{40}Ar and $^{40}Ar/^{39}Ar$ analysis of potassium-manganese oxides. Science 258, 451–455.
Vasconcelos, P.M., Renne, P.R., Brimhall, G.H., Becker, T.A., 1994. Direct dating of weathering phenomena by $^{40}Ar/^{39}Ar$ and K–Ar analysis of supergene K–Mn oxides. Geochimica et Cosmochimica Acta 58, 1635–1665.
Vasconcelos, P.M., Renne, P.R., Becker, T.A., Wenk, H.-.R., 1995. Mechanisms and kinetics of atmospheric, radiogenic, and nucleogenic argon release from cryptomelane during $^{40}Ar/^{39}Ar$ analysis. Geochimica et Cosmochimica Acta 59, 2057–2070.
Villalobos, M., Bargar, J., Sposito, G., 2005. Trace metal retention on biogenic manganese oxide nanoparticles. Elements 1 (4), 223–226.
Zouiten, S., 1999. Application de la géothermométrie chimique aux eaux des sources thermales du Nord de la Tunisie. Unpublisched PhD thesis, Tunis II University, 197p.